



Comparison of Ozone Monitoring Instrument UV Aerosol Products with Aqua/Moderate Resolution Imaging Spectroradiometer and Multiangle Imaging Spectroradiometer observations in 2006

Changwoo Ahn,¹ Omar Torres,^{2,3} and Pawan K. Bhartia^{3,4}

Received 13 April 2007; revised 10 December 2007; accepted 28 January 2008; published 20 May 2008.

[1] An assessment of the consistency of the Ozone Monitoring Instrument (OMI) aerosol products with the results from other satellite aerosol sensors is performed in this paper. The OMI aerosol products include the UltraViolet Aerosol Index (UVAI), Aerosol Absorption Optical Depth (AAOD), and Aerosol Extinction Optical Depth (AOD). The OMI AOD is compared with that from Aqua/Moderate Resolution Imaging Spectroradiometer (MODIS) and Terra/Multiangle Imaging Spectroradiometer (MISR). OMI-retrieved AOD values are generally biased high with respect to MODIS measurements, likely as a result of a calibration offset. Subpixel cloud contamination is the second most important source of error. Other sources of error may contribute to the noise in the retrieval but not necessarily to the systematic bias. In spite of the bias, OMI retrievals show a high degree of correlation with MODIS observations. The analyses of daily cloud-free collocated AOD data between OMI and MODIS show about 0.15 root mean square error on average relative to the linear fit. OMI also shows a reasonable agreement with MODIS and MISR observations in seasonal annual cycles of aerosols over most of the major emission sources of carbonaceous aerosols from biomass burning and mineral dust from deserts. The AAOD is less sensitive to cloud contamination than the AOD. In addition, the information content in the UVAI is well expressed as AAOD with higher correlation than AOD. However, subpixel cloud contamination of OMI footprint ($13 \times 24 \text{ km}^2$ at nadir) is unavoidable, and retrieved AOD values tend to be overestimated with varying degrees of sensitivity as a function of viewing geometry and aerosol types selected.

Citation: Ahn, C., O. Torres, and P. K. Bhartia (2008), Comparison of Ozone Monitoring Instrument UV Aerosol Products with Aqua/Moderate Resolution Imaging Spectroradiometer and Multiangle Imaging Spectroradiometer observations in 2006, *J. Geophys. Res.*, 113, D16S27, doi:10.1029/2007JD008832.

1. Introduction

[2] Absorbing aerosols such as carbonaceous aerosols from biomass burning and boreal forest fires, and desert dust lofted by the winds from the world major arid and semiarid areas are among the most long-lived aerosol types in the Earth's atmosphere since they often reach the free troposphere and are sometimes transported thousands of kilometers from their original sources. These aerosols interact with other aerosol types such as urban industrial pollutants and sulfate during the period of transport under various meteorological conditions. As a result of this interaction a complex composition of mixed type aerosols may result and

affect the radiative balance of the climate system both directly (absorption and scattering of incoming solar radiation) and indirectly (modifying microphysical properties and lifetimes of clouds). Analysis of aerosol absorption data from the world wide Aerosol Robotic Network (AERONET) of ground-based radiometers over an 8-year period shows significant spatial and temporal variability. The observed variability in absorption for the same aerosol type is associated with different meteorological conditions and source characteristics as well as different emission strengths [Dubovik *et al.*, 2002]. Such a high heterogeneity and variability of absorbing aerosols over time and space requires daily continuous long-term global observations from satellites [Kaufman *et al.*, 1997; King *et al.*, 1999; Torres *et al.*, 1998]. Despite important advances in the understanding of the role of absorbing aerosols, the quantification of particle absorption effects on the climate system remains highly uncertain. The current limited knowledge of these processes is due to both incomplete understanding of the physical and chemical processes driving the complex climate system, and limited observations from space with global coverage. The

¹Science Systems and Applications, Inc., Lanham, Maryland, USA.

²Goddard Space Flight Center, NASA/University of Maryland, Greenbelt, Maryland, USA.

³Now at Department of Atmospheric and Planetary Sciences, Hampton University, Hampton, Virginia, USA.

⁴Goddard Space Flight Center, NASA, Greenbelt, Maryland, USA.

advent of modern remote sensing instruments such as Moderate Resolution Imaging Spectroradiometer (MODIS) and Multiangle Imaging Spectroradiometer (MISR) with advanced algorithms has ushered in a new era of global aerosol remote sensing. However, no single sensor system is capable of providing totally unambiguous information about our quantitative understanding of global aerosol characteristics [King *et al.*, 1999].

[3] For the past 25 years, NASA's Total Ozone Mapping Spectrometer (TOMS) series of instruments have made great contributions to the observation of the global distribution of aerosol sources, and the transport patterns of UV absorbing aerosols by making use of the near-UV observations to map the global distribution in terms of an Aerosol Index [Herman *et al.*, 1997] as well as aerosol optical depth [Torres *et al.*, 2002a]. Because both smoke and desert dust aerosols absorb UV radiation, the near-UV aerosol sensing technique is specially suited for tracking these aerosol types over all terrestrial surfaces even when covered by ice or snow, and above clouds.

[4] We have recently completed the development of an improved algorithm to retrieve both aerosol extinction optical depth (AOD) and aerosol absorption optical depth (AAOD) using near-UV measurements from the Ozone Monitoring Instrument (OMI) sensor on the EOS Aura satellite. A detailed description of the characteristics of the sensor is given by Levelt *et al.* [2006].

[5] In a separate paper O. Torres *et al.* (manuscript in preparation, 2008) have evaluated the OMI retrieved quantities using ground-based observations by AERONET. In this paper, we compare OMI retrieved AOD with that of Aqua/MODIS and Terra/MISR observations of the same parameters. These two data sets have fairly reliable cloud screening techniques that take advantage of their fine spatial resolution. MODIS and MISR aerosol optical depth retrievals have been validated using AERONET measurements over the oceans and the continents [Chu *et al.*, 2002; Kahn *et al.*, 2005; Kaufman *et al.*, 1997; Abdou *et al.*, 2005]. From a viewpoint of global comparison, these are adequate data sets with sufficient spatial and temporal coverage for the evaluation of the lower spatial resolution OMI aerosol data with a footprint of $13 \times 24 \text{ km}^2$ at nadir.

[6] In section 2 a brief description of the OMI aerosol data used in the analysis is presented. In the following sections, sample daily images of the OMI UV aerosol products over a variety of locations with interesting aerosol events in 2006 are illustrated to assess qualitatively the advantages and disadvantages of the OMI aerosol product. In section 5, 6, and 7, daily/monthly AOD comparisons over these selected regions are made with MODIS and MISR, followed by a further discussion of future improvement of OMI aerosol products in conjunction with additional information from other A-train sensors.

2. Description of OMI Aerosol Data Set

[7] The OMI UV aerosol product (Aura OMI Aerosol Data Product (OMAERUV) Collection 2) is now publicly available at the Goddard Earth Sciences Distributed Active Archive Center (http://disc.sci.gsfc.nasa.gov/data/dataset/OMI/Level2_V003/OMAERUV/). (Collection 3 data was

not available when preparing this paper, however, currently Collection 3 data is available and linked to the given web site.) The near UV method of aerosol characterization uses space measurements at two channels in the near UV to detect aerosol absorption. The Aerosol Index is the most widely known near UV aerosol product. It is a qualitative parameter that indicates the presence in the atmosphere of UV light absorbing particles on the basis of the radiative interaction between molecular scattering and particle absorption. In addition to the aerosol physical and optical properties, the AI also depends on the height of the aerosol layer above the ground [Torres *et al.*, 1998]. Because of its dependence on height the AI's sensitivity is largest for elevated (at least 2 km above the surface) aerosol layers, and decreases rapidly with aerosol layer height. The AI's loss of sensitivity with height is particularly large for gray aerosols, making very difficult the separation of absorbing and nonabsorbing aerosols in the boundary layer. On the other hand, the AI is sensitive to colored aerosol layers down to a few hundred meters above the surface [Mahowald and Dufresne, 2004]. The quantitative characterization of absorbing aerosols is carried out using an inversion procedure that uses as input the measured radiances at two near UV channels, to derive AOD and single scattering albedo (SSA) at 388 nm. Retrieved values of AOD and SSA are converted to 354 and 500 nm making use of the spectral dependence associated with the assumed aerosol models [Torres *et al.*, 2007]. Since the aerosol models are based on multiyear AERONET statistics [Torres *et al.*, 2002a, 2007], realistic wavelength dependence is expected as the spectral conversion is basically based on AERONET observations. Subpixel cloud contamination produces an AOD overestimation, and an underestimation of the single scattering albedo ($1.0 - \text{SSA}$). As a consequence, in the calculation of AAOD a partial cancellation of errors takes place. Thus, the calculated AAOD is less sensitive to low amounts of subpixel cloud contamination than either AOD or SSA separately. The retrieved AAOD is more sensitive than the AI to boundary layer aerosols. A more detailed description of the OMI UV aerosol retrieval algorithms is presented by Torres *et al.* [2007]. The level 2 file contains AOD, and AAOD at three wavelengths (354, 388, and 500 nm), UV Aerosol index (UVAI), and ancillary parameters such as aerosol types, aerosol layer height, and surface albedo. The level 2 file also has a data field called as "Algorithm flag" to provide a guideline of screening the cloud-contaminated AAOD and AOD scenes. The interpretation and criteria for each flag category expressed as an integer number summarized in Table 1. The categories are mutually exclusive, and apply to both absorbing and nonabsorbing aerosol types. The parameters UVAI and ΔR are used in the determination of the levels of subpixel cloud contamination associated with the AAOD and AOD [Torres *et al.*, 2007]. The quantity ΔR is the net aerosol-related 388 nm reflectivity change, calculated as the difference of ($R_{\text{obs}} - R_{\text{sfc}}$), where R_{obs} is the observed Lambert equivalent reflectivity and R_{sfc} is the surface albedo. The AOD is sensitive to both scattering and absorption effects while the AAOD is only sensitive to absorption. Therefore, the AAOD is less sensitive to small amounts of cloud contamination than the AOD. Three aerosol types (smoke, dust, and sulfate) are identified with a decision rule of multiple criteria including

Table 1. Interpretation and Criteria for the Algorithm Flag in OMAERUV Level 2 File

Flag Value	Interpretation	Criteria	Recommendation
0	Minimum cloud contamination	UVAI > 1.2 and $\Delta R \leq 0.05$; UVAI ≤ 1.2 and $\Delta R \leq 0.03$	Both AOD and AAOD can be use with confidence.
1	Minimum cloud interference in AAOD	UVAI ≥ 1.2 and $R_{\text{obs}} < 0.30$	AAOD is considered reliable; AOD is cloud contaminated.
2	Both AOD and AAOD are less reliable	UVAI < 1.2 and $0.03 < \Delta R < 0.08$	Cloud contamination likely; use with caution.
3	Retrieved values out of bounds	Extrapolation in look-up tables	Do not use.
4	Cloud, snow, or ice contamination	Conditions not met for flag categories 0, 1, and 2	Do not use.
5	Solar zenith angle above threshold	SZA > 70°	No retrieval.
6	Sun glint contamination (water surfaces)	Sun glint angle < 40°	No retrieval.
7	Terrain pressure below threshold	$P_0 < 628.7$ hPa	No retrieval.

UVAI, ΔR , and the International Geosphere/Biosphere Programme (IGBP) scene type data [Torres *et al.*, 2007].

3. Sample OMI Retrievals of UVAI, AAOD, and AOD

[8] Figures 1–4 depict OMI retrieved UVAI, AOD and AAOD over selected regions of the world. The white box overlaid on the AOD images represents the spatial coverage of Aqua/MODIS granule to be collocated with OMI for AOD comparison later in section 5. The OMI aerosol products with a grid size of $0.25^\circ \times 0.25^\circ$ are projected on NASA’s blue marble background to illustrate their relationships in terms of spatial patterns and magnitudes. The UVAI images shows all values above 1.0 indicating mostly elevated UV absorbing aerosols even over clouds. The 388 nm AAOD image is constructed with data of flag 0, 1, and 2. The 388 nm AOD images are made from data of flag 0 and 2. Therefore, spatial coverage from AAOD and AOD can be different because of the degree of cloud screening. The smoke plume detected by the OMI UVAI over the sub-Saharan region of West Africa on 2 January 2007 is shown in Figure 1a. Characterization of aerosol properties from space over this region is a challenging task because of the frequent interference of thick clouds and the presence of mixtures of smoke from biomass burning and mineral dust flow from the Saharan desert. Therefore, the identification of a single aerosol type is a difficult task in this region. The areas of large UVAI values shown as yellow and red colors near the Sahelian region in the map are associated with westward wind-blown dust from the Lake Chad region. In the sub-Saharan region, smoke generated by biomass burning from anthropogenic activities is shown as blue and green color (confirmed by MODIS fire counts real-time image and NCAR/NCEP vector winds map at 850 hPa for that day, though not shown here). The AAOD image in Figure 1b shows values of about 0.15 (green) – 0.20 (yellow) near the sources of emission. The areas of highest value about 0.3 with red/pink colors could be mixtures of aerosols with clouds. However, a large portion of AAOD scenes corresponding to high UVAI scenes (yellow/red color in Figure 1a) is removed because of high levels of cloudiness. Further scenes are filtered out by excluding flag 1 data for the AOD image in Figure 1c that shows values of about 1.0 (green) near the sources of emission.

[9] Figure 2a shows the UVAI image of the accumulated desert dust mixed with urban pollutants over the northern

part of the Indian subcontinent, along the slopes of the Tibetan Plateau on 14 May 2006. Much attention has been drawn over this region associated with growing population, rapid urbanization, and topography that confines heavy absorbing aerosols in the Ganga basin surrounded by mountains throughout the entire year [Di Girolamo *et al.*, 2004]. The UVAI over this region was used as a good proxy for tracking the change of Asian monsoon water cycle in support of the “elevated heat pump” effect due to a large absorption of solar radiation of absorbing aerosols [Lau and Kim, 2006]. They demonstrated that heavy loading of absorbing aerosols detected by the TOMS Aerosol Index over the Indo-Gangetic Plain in the premonsoon season is associated with increased heating of the upper troposphere, and an advance of the monsoon rainy season in northern India in May [Lau and Kim, 2006]. A more direct quantification of the absorbed UV solar radiation at 388 nm is obtained in terms of the AAOD as shown in Figure 2b. In this case, the highest UVAI values in the range of 4–5 in Figure 2a are well correlated with high AAOD values of 0.2–0.3 in Figure 2b. However, caution must be taken in the interpretation of the UVAI as its magnitude is enhanced when the aerosol is located above clouds. A high UVAI (i.e., above 1.0) is generally associated with a combination of elevated aerosols, higher extinction optical depth, and absorption properties. UVAI values below 1.0 are difficult to interpret as actual aerosol signal because of the background noise present at low AI values. Figure 2c shows the AOD image with Aqua/MODIS granule outline after screening heavily cloud-contaminated scenes.

[10] A heavy dust storm that swept through east Asia including China and Korea on 10 March 2006 is well captured in Figure 3a. The dust storm originated in the Taklamakan desert. It traveled through the Gobi desert, urban areas in mainland China, and the Korean peninsula. Corresponding AAOD and AOD images in Figures 3b and 3c are shown for comparison. Both AAOD and AOD images also contain information of smoke type aerosols from fires over south east Asia.

[11] Aerosol events associated with dust flow from the Saharan desert and biomass burning in Central Africa on 15 August 2006 are depicted in Figure 4. It clearly illustrates two types of absorbing aerosols; a dust storm from the Saharan desert, and a smoke plume from biomass burning in central and southern Africa. Over ocean, a large portion of

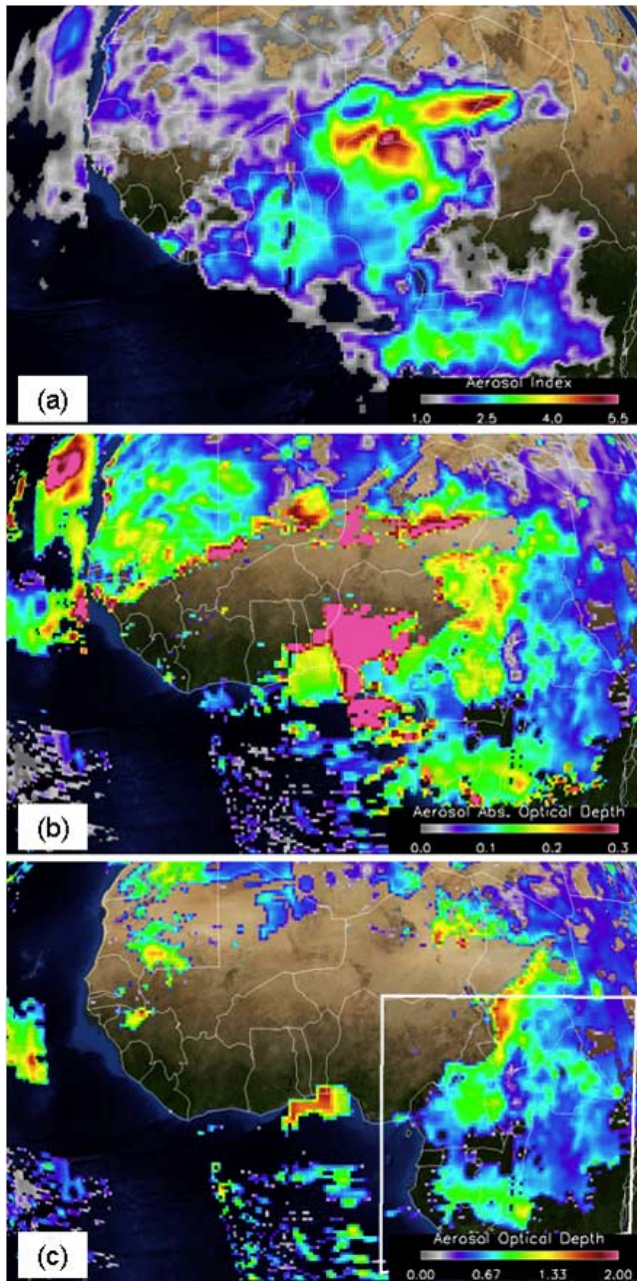


Figure 1. (a) OMI UVAI, (b) AAOD, and (c) AOD images for a smoke plume over the Sahelian region in West Africa on 2 January 2007. The white box in the AOD image (Figure 1c) represents a granule boundary of Aqua/MODIS for collocation study in Figure 6. The differences of spatial coverage among three data sets are due to the degree of cloud screening with algorithm flags. The detailed methods are described in the text. The NASA's blue marble image is used as a base map.

data is prescreened because of the sun glint interference in the retrieval.

4. Intercomparison of OMI UVAI, AOD, and AAOD

[12] As a qualitative measure of absorbing aerosols the UVAI is correlated with the actual aerosol amounts

expressed in terms of optical depth. The UVAI-AOD (and AAOD) relationships depend on the specific properties of the aerosol and the height of the absorbing layer [Hsu et al., 1999]. The resulting relationships for desert dust aerosols are illustrated in Figure 5. Figures 5a and 5b show scatterplots of the UVAI and the AOD and AAOD, respectively. The data in the plot includes a region over the

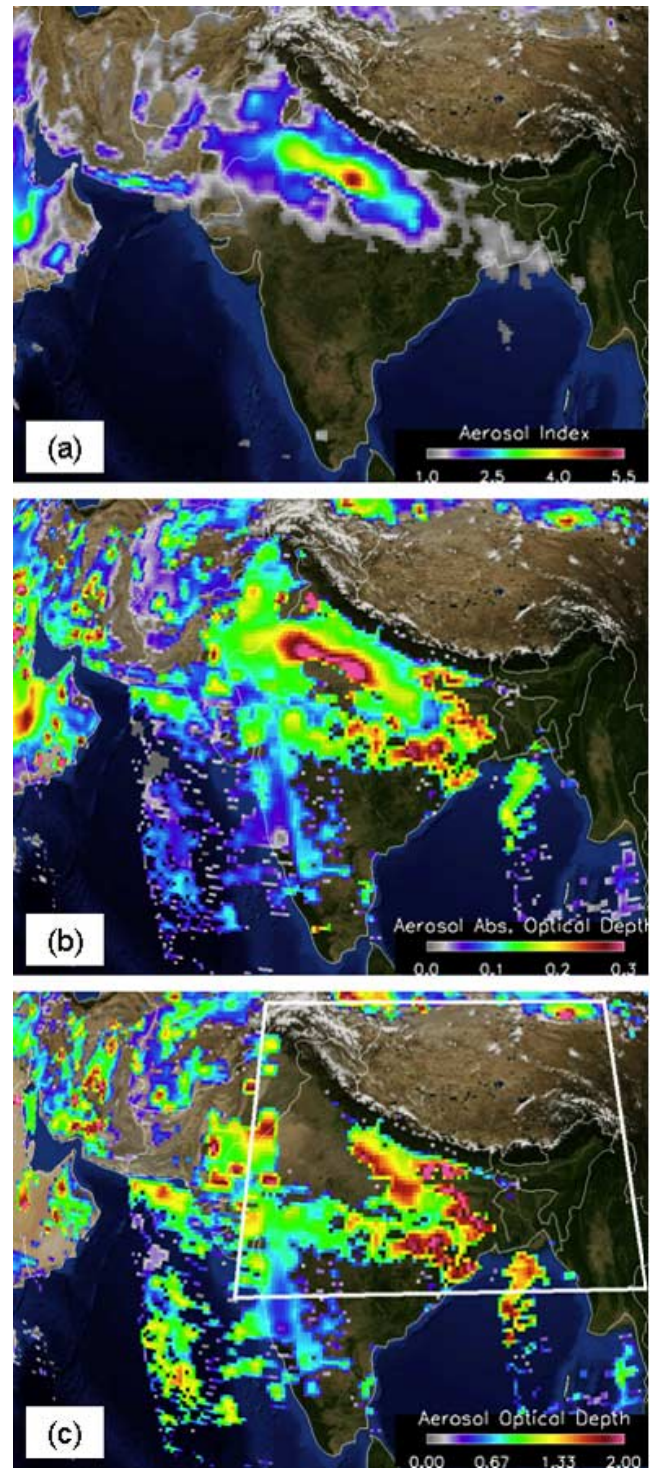


Figure 2. Same as Figure 1 except for a mixture of dust/industrial pollutants over Indian subcontinent on 14 May 2006.

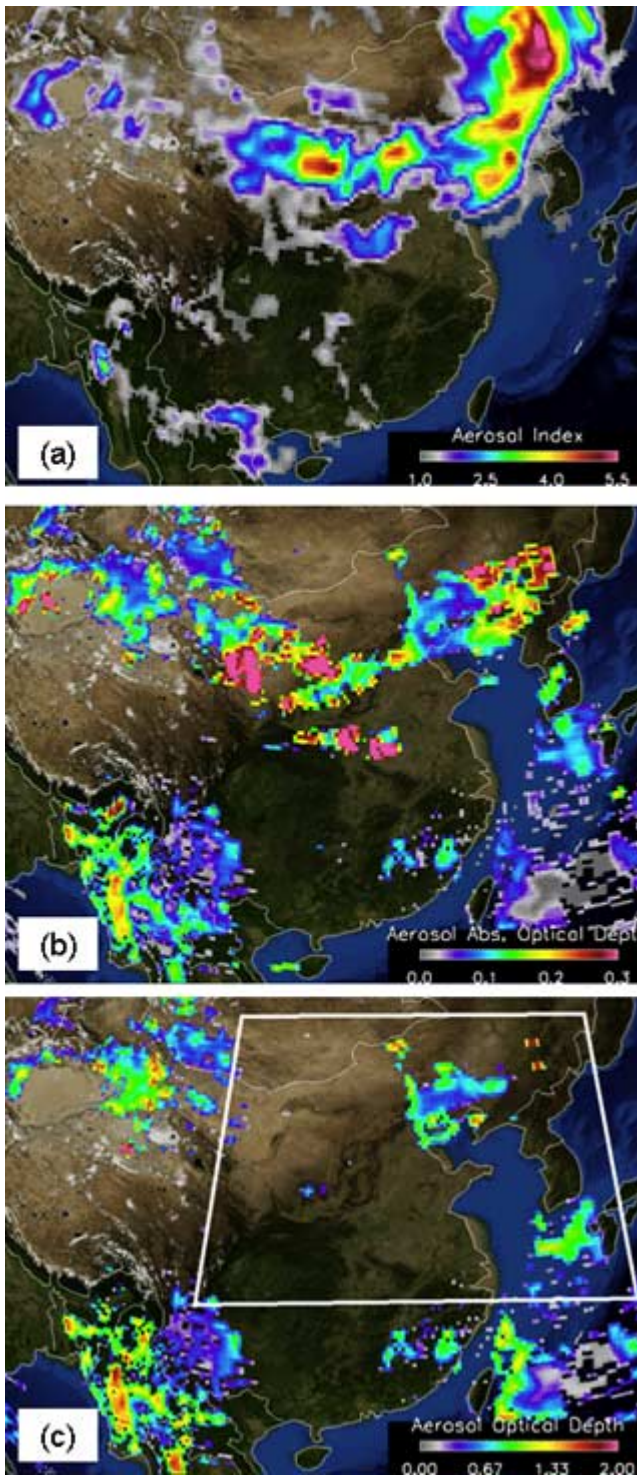


Figure 3. Same as Figure 1 except for a mixture of dust storm and smoke over east Asia on 10 March 2006.

Saharan desert region (10°W–30°E, 15–30°N) on 15 August 2006 (Figures 5a and 5b), a typical day of peak summer seasonal dust loading. As expected, a high correlation between the UVAI and the retrieved parameters is observed during the summer when large aerosol loads are present and cloud interference with the retrieval is minimum. A higher correlation coefficient (0.84) is observed

for the UVAI-AAOD relationship than for the UVAI -AOD comparison (0.75). A similar analysis is presented in Figures 5c and 5d over the same region on 29 November 2006, a typical day of lesser amounts of dust load in winter season over this region. In Figure 5c, a distinct step change of AOD is found at UVAI of 1.2 where ΔR threshold in the algorithm flag 0 is changed from 3% (when UVAI below 1.2) to 5% (when UVAI above 1.2). This increase of 2% reflectivity results in about 20% increase in AOD for some cloud contaminated scenes, but, apparently, not in AAOD,

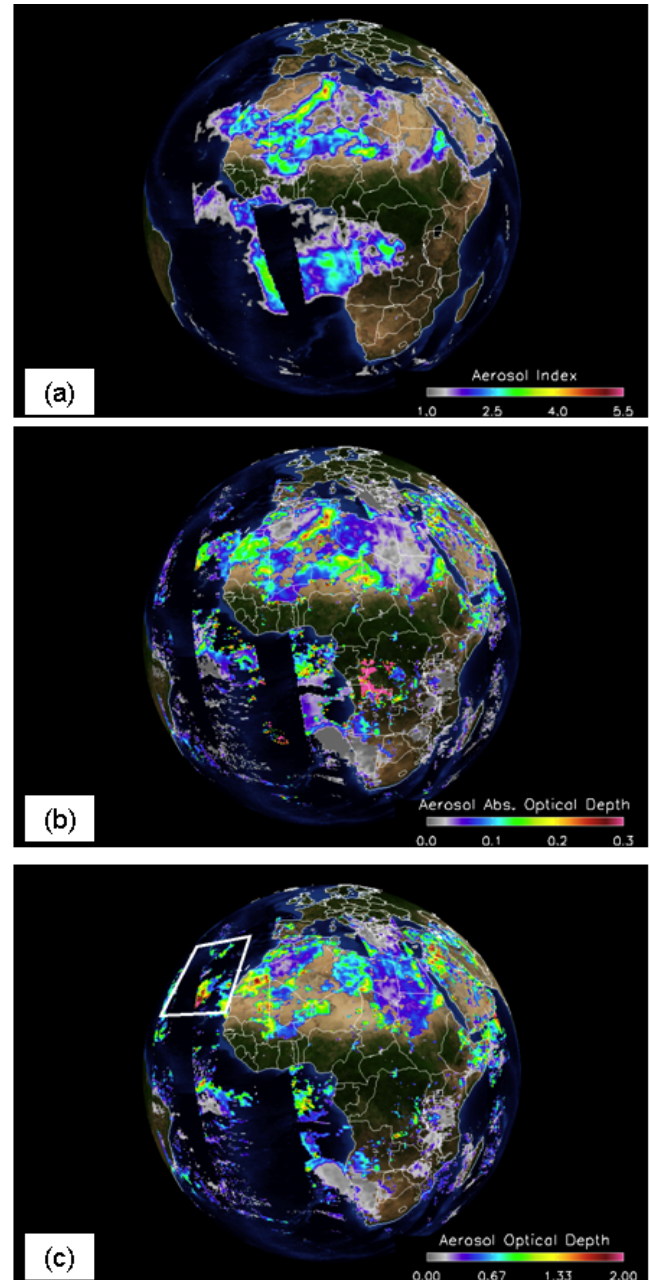


Figure 4. Same as Figure 1 except for two distinct types of aerosols, a dust storm from the Saharan desert, and a smoke from biomass burning in South Africa on 15 August 2006.

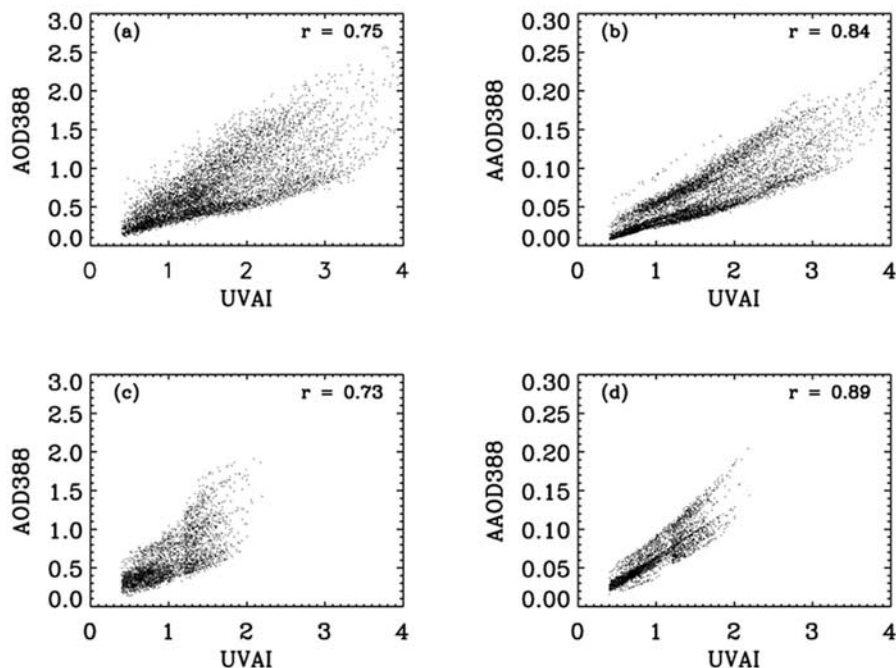


Figure 5. Scatterplots of OMI AOD and AAOD against UVAI over the Saharan desert region (10°W – 30°E , 15 – 30°N) for (a and c) 15 August 2006 and (b and d) 29 November 2006, respectively. The correlation coefficient (r) is also shown in each plot.

which confirms that AAOD is less affected by clouds than AOD as expected since clouds enhance the scattering effect but not the absorption. Therefore, AAOD is less sensitive to low levels of subpixel cloud contamination than AOD. As a result, the change of reflectivity can cause some degree of cloud contamination particularly for low aerosols loaded days/areas, though it does not have much effect on AAOD. A tighter constrain of ΔR helps reduce cloud contamination effects in AOD but also sacrifices good quality AAOD data to some extent. Therefore, care should be taken to address this trade-off that depends on specific applications.

5. Comparison of OMI With Collocated Aqua/MODIS AOD Data

[13] The Aqua satellite is the lead spacecraft in the formation of the Afternoon satellite constellation known as the “A-Train.” The Aura/OMI lags Aqua/MODIS by about 15 minutes. The feature of nearly concurrent measurements from the two spacecrafts in time and space enables us to compare aerosol products precisely with the minimum number of collocated data on a few granule basis. A linear interpolation and extrapolation technique between each OMI center geolocation is used for estimating the approximated corner geo-coordinates of the OMI pixels. The 550 nm AOD data of Aqua/MODIS Level 2 product (Collection 5 MYDATML2) with 10 km resolution falling into corresponding OMI footprints are averaged and compared with the 500 nm OMI AOD values. The 388–500 nm wavelength conversion is carried out as described in section 2. MODIS quality assurance flag 2 (good) and 3

(very good) are used for this comparison. Spatial coverage of collocated regions is shown as white rectangles in Figures of 1c, 2c, 3c, and 4c. Collocated granules are designated as A (sub-Sahel), B (Indian subcontinent), C (China), and D (Atlantic Ocean) in Figure 6 for the corresponding days of Figures 1–4 in that order. The comparison in all four cases shows that although there is a high degree of correlation between the MODIS and OMI retrievals, the OMI measurements are consistently higher than those of MODIS with intercept values of 0.18, 0.49, 0.29 and 0.26, respectively. Such offset could be the result of a systematic overestimation of the surface albedo, a calibration error or a combination of these two effects. The magnitude of the offset, however, is too large to be explained solely as a surface albedo effect. Thus, we believe the offset is mainly a calibration related artifact, although the effect of subpixel cloud contamination is likely present as a second-order effect. A new Level 1b data set of calibrated radiances (Collection 3) has recently been produced and the entire OMI aerosol record will be reprocessed. (As clarified in section 2, Collection 3 data is now publicly available.) Generally, both OMI and MODIS AOD agree within 0.15 root mean square error of the obtained regression lines. In spite of the offset OMI retrievals show consistency with the MODIS measurements with correlation coefficients of 0.67, 0.72, 0.78 and 0.66 for the four cases in the analysis. In Figure 6c, the collocated granule over coastal zones of the Bohai Gulf in China for 10 March (see also Figure 3c), MODIS AOD data above 1.0 is excluded in the linear fitting procedure and computing the correlation coefficient because unusually high MODIS AOD is due to the well-known issue of surface inhomoge-

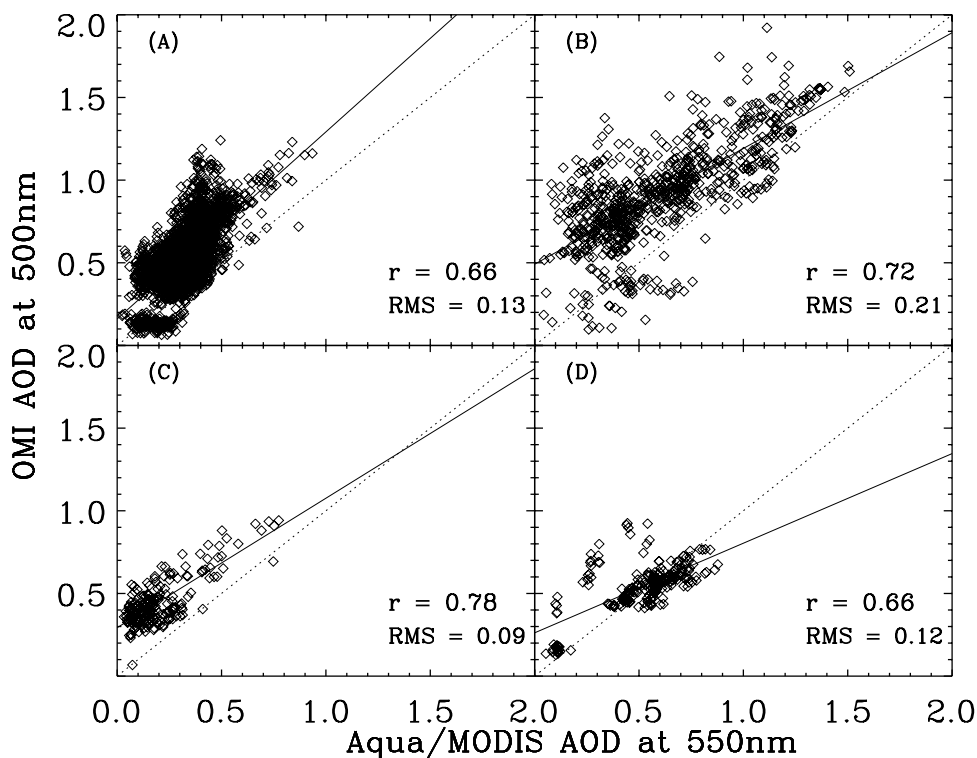


Figure 6. Scatterplots between collocated Aqua/MODIS 550 nm AOD and OMI 500 nm AOD with algorithm flag 0 for the following 4 selected days: (a) 2 January 2007 over the smoke plume in the sub-Saharan region of West Africa, (b) 14 May 2006 over the accumulated dust of the Ganga basin in Indian subcontinent, (c) 10 March 2006 over the dust storm in China, and (d) 15 August 2006 over the dust storm from the Saharan desert. The dotted lines indicate the one-to-one, and the solid lines are the linear fitted ones. The root mean square (RMS) error and correlation coefficient (r) are shown in each AOD comparison. For Figure 6c, MODIS AOD data above 1.0 is excluded in the linear fitting procedure and computing the correlation coefficient because of the reason explained in the text. The slopes (a) and intercepts (b) of the linear fit equation for each day are as follows: Figure 6a, $a = 1.09$ and $b = 0.18$; Figure 6b, $a = 0.70$ and $b = 0.49$; Figure 6c, $a = 0.78$ and $b = 0.29$; Figure 6d, $a = 0.54$ and $b = 0.26$.

neity or water contamination for MODIS aerosol retrieval [Chu *et al.*, 2002]. The observed noise in the comparison is probably associated with collocation errors or OMI algorithm related factors such as prescribed aerosol layer height and misidentified aerosol types.

[14] In Figure 7, the MODIS 550 nm AOD is also compared qualitatively with the OMI 388 nm AAOD of flag 0 and 1. The comparison clearly shows different clusters indicating different types of aerosols with different single scattering albedo. Slope of each cluster is equal to $(1.0 - SSA)$. Therefore, clusters of higher slopes are normally associated with highly absorbing smoke aerosols. On the other hand, clusters of lower slopes are associated with dust type aerosol. No slope indicates nonabsorbing type aerosols. Some of the high AAOD values might be the result of mixtures of clouds with aerosols. Plots corresponding to regions A and B display retrievals closer to emission sources. Over these regions stronger absorption associated with both smoke and dust aerosols is observed than the results shown for regions C and D, where thin dust aerosol layers transported from the source

regions appear to be dominated by local smoke aerosols. Such a high variability of mixtures of fine and coarse mode aerosols in time and space is commonly observed from a combination of factors including aerosol aging during transport, relative humidity differences, sea salt at coastal sites, and fuel type and combustion differences [Eck *et al.*, 2005].

6. Global Monthly Average AOD and AAOD From OMI Observations

[15] The OMI global monthly average maps of 0.5° grid size for AAOD (using flag 0 and 1 data) and AOD (flag 0 only) in 2006 are made using a minimum of 2 days per month, and selected four months are shown in Figure 8. Full coverage over the major arid and semiarid areas of the world is achieved for both products. Observed gaps are associated with persistent cloud contamination. The well-known seasonal patterns of aerosol distribution are reproduced. In particular, AAOD maps show biomass burning regions in equatorial Africa in January and Southern Africa

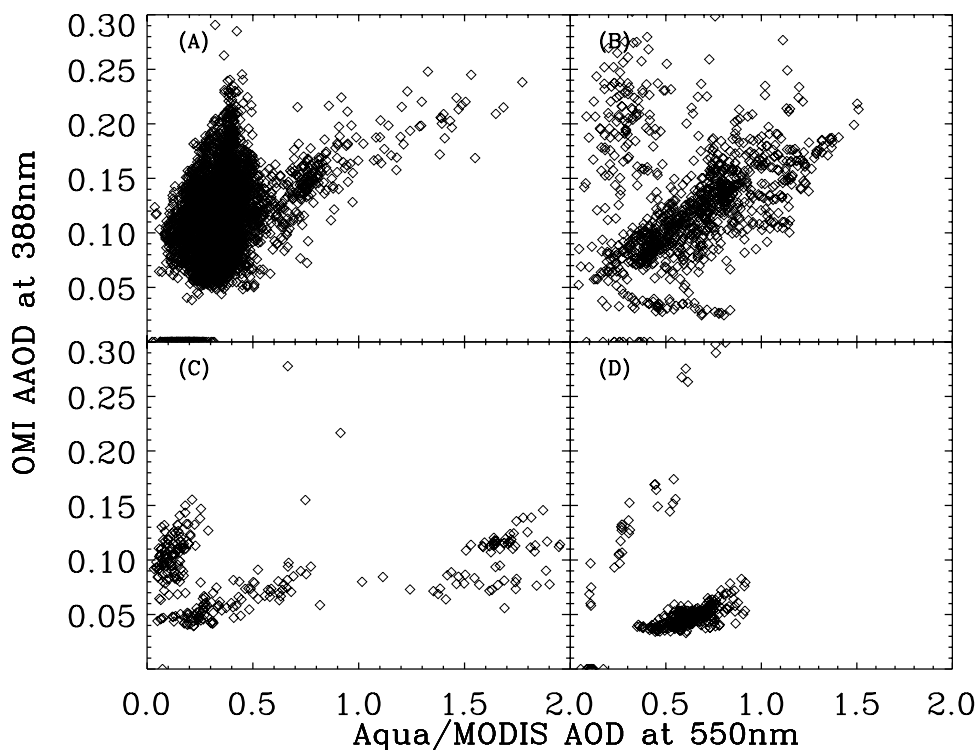


Figure 7. Scatterplots between collocated Aqua/MODIS 550 nm AOD and OMI 388 nm AAOD with algorithm flag 0 and 1 for the following 4 selected days: (a) 2 January 2007 over the smoke plume in the sub-Sahel region of West Africa, (b) 14 May 2006 over the accumulated dust of the Ganga basin in Indian subcontinent, (c) 10 March 2006 over the dust storm in China, and (d) 15 August 2006 over the dust storm from the Saharan desert.

in July, and central South America in September. Significant aerosol absorption in the near-UV with AAOD values as large as 0.15–0.25 is observed over China in January. These high aerosol absorption levels are probably the results of aerosol mixtures involving desert dust and industrial pollution as well as smoke from biomass burning. Another significant feature of high aerosol absorption associated with carbonaceous smoke from Siberian wild fires can be clearly seen in the July AAOD map. Figures 9a and 9b show monthly average maps of the OMI retrieved 388 nm single scattering albedo over Africa and the Atlantic Ocean for January and July 2006. Similar maps for SSA converted to 500 nm are shown in Figures 9c and 9d. During these months cloud contamination interference is minimum over Northern Africa and the area of influence of the Saharan dust layer. This region was chosen because it exhibits the most marked seasonal contrast in terms of aerosol absorption properties. The SSA maps are constructed with flag 0 and 1 of the minimum of 2 days per month in making monthly averages at 0.5° grid size.

[16] The January map (Figure 9a) shows a distinct aerosol feature confined to a latitudinal belt between 10° and 15° . These are highly absorbing aerosols with SSA values as low as 0.82, associated with intense biomass burning and possibly mixed with dust. As the smoke plume drifts westward over the Atlantic Ocean and into the southern hemisphere, the SSA increases to values as high as 0.92. Given the hygroscopic nature of carbonaceous aerosols the observed SSA increase as the smoke plume ages is expected. The SSA over the Saharan desert in January is

about 0.89 and shows little spatial variability. In July (Figure 9b) when there is no biomass burning activity in Northern Africa, the Saharan dust layer is clearly observed as it travels from the continent across the Atlantic Ocean. SSA values in the range 0.88–0.94 are observed over land. An average value of about 0.93 is observed over the ocean without much spatial variability. Figures 9c and 9d depict the 500 nm converted values. As expected, the SSA of the biomass burning aerosols shows little spectral dependence whereas dust appears less absorbing in the visible than in the near UV.

7. Seasonal Variability of Monthly AOD From OMI, MODIS, and MISR

[17] A comparison of the annual variability of the atmospheric aerosol load as retrieved by the OMI, MODIS and MISR sensors over major aerosol source regions is presented in this section. For a more precise comparison with MODIS and MISR, monthly OMI gridded products are made with the criteria of flag 0 and ΔR below 0.03, instead of utilizing flag 0 only since it can reduce a possible cloud contamination due to the change of ΔR in the current criteria of algorithm flag 0, as seen in Figure 5.

[18] The six regional boxes over the world shown in Figure 10 were chosen for comparison of seasonal annual cycles of aerosols as following: A is the northern African desert (10°W – 30°E , 15° – 30°N), B is the Arabian peninsula (38° – 60°E , 15° – 33°N), C is east Asia (100° – 140°E , 30° – 50°N), D is the Indian subcontinent (60° – 100°E , 15° – 30°N),

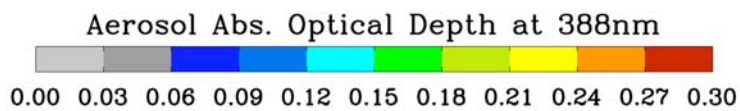
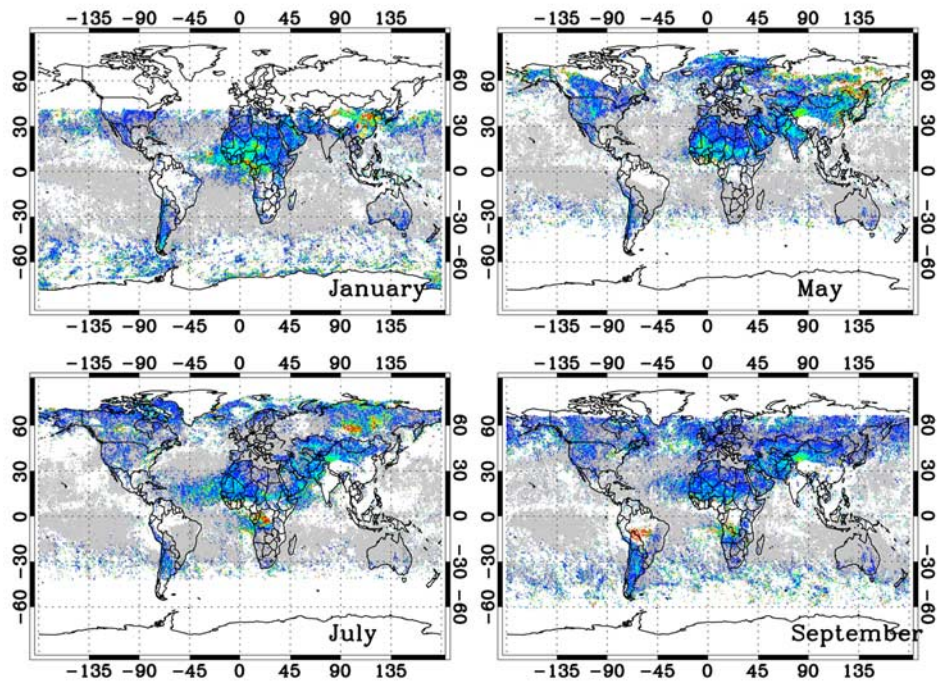
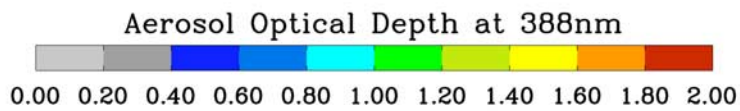
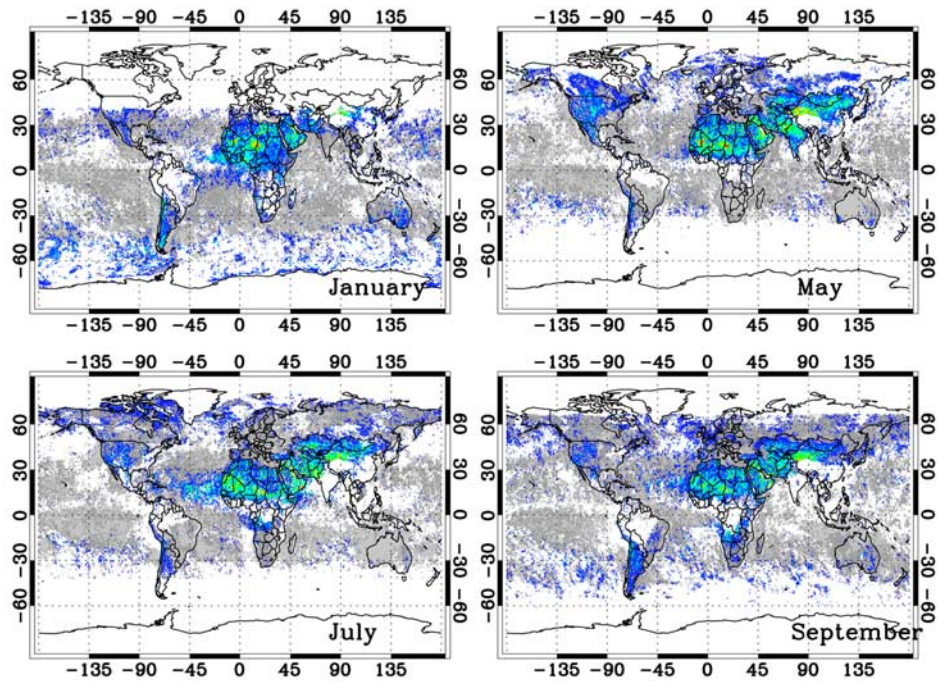


Figure 8. AOD and AAOD monthly maps for January, May, July, and September in 2006. The AOD maps are constructed with flag 0 only, but AAOD maps with flag 0 and 1. Both maps have the minimum of 2 days per month in making monthly averages at 0.5° grid size.

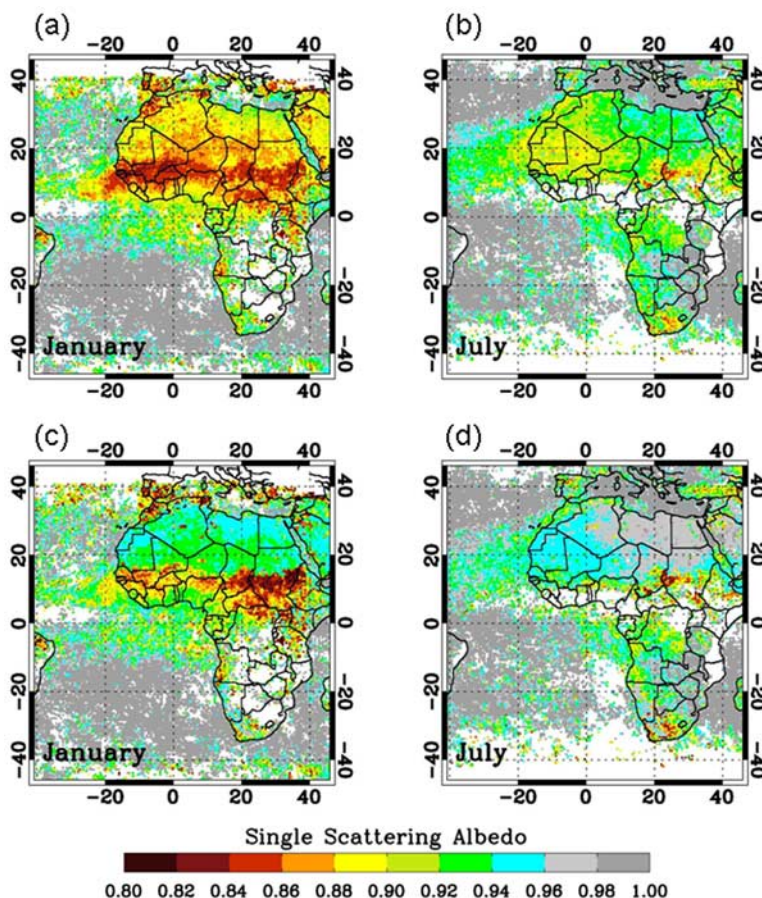


Figure 9. Monthly average maps of 388 nm SSA over the African continent and Atlantic Ocean for (a) January and (b) July in 2006. (c and d) Converted values to 500 nm are also shown.

E is equatorial West Africa (20°W – 20°E , 18°S – 10°N), and F is South America (80 – 40°W , 0 – 20°S). The level 3 monthly AOD gridded products of MISR (MISR_AM1_CGAS) and MODIS (Collection 005 MYD08_M3) are obtained from the NASA Langley Research Center Atmospheric Science Data Center, and Goddard Space Flight Center Level 1 and Atmosphere Archive and Distribution System (LAADS), respectively.

[19] In spite of many differences among three instruments such as spatial coverage, observational strategy, retrieval scheme, and radiometric calibration, generally, AOD from three instruments shows a fairly good agreement in seasonal cycles of typical aerosols over a variety of regions. The resulting annual AOD cycles for the selected regions are shown in Figure 11.

[20] In region A including the Saharan desert, the largest source of mineral dust in the world, the three instruments show the peak AOD in June and the minimum in November. Monthly MODIS AOD shown here is from the deep blue products because the standard MODIS aerosol product does not retrieve aerosol information over bright surfaces due to a strong surface spectral contribution in the visible [Kaufman *et al.*, 1997]. Recently, however, a new algorithm, called “Deep Blue algorithm” [Hsu *et al.*, 2006], has been integrated with existing MODIS algorithm to retrieve

AOD even over bright surfaces such as deserts. The deep blue products are as being validated yet. Although, MISR retrieves AOD with acceptable accuracy it can miss daily dust storm events or sources of emission (i.e., dry lakebed of Lake Chad) because of its narrow viewing swath (360 compared to 2600 km of OMI), and can be underestimated in this region in a monthly aggregate.

[21] OMI retrievals over the Saharan desert (region A) are consistently larger than those of MISR and MODIS, although the seasonal patterns are similar. In the summer months, when the aerosol lifting activity is strongest in the region, OMI is about 0.1 larger than MISR. However, MODIS AOD is significantly lower than OMI and MISR in the summer months (July and August). In the winter, OMI is significantly larger than MISR and MODIS. The low MISR and MODIS winter values are in agreement with the long-term climatological record from TOMS [Torres *et al.*, 2002a]. In early months from January through June, MODIS shows a reasonable agreement with MISR that may have sampling limitations. Therefore, we need a further validation to assess the OMI AOD retrievals in this region with ground-based measurements, although such observations are very limited over the Saharan desert.

[22] Over the Arabian Peninsula (region B) where mixtures of industrial pollution with transported mineral dust

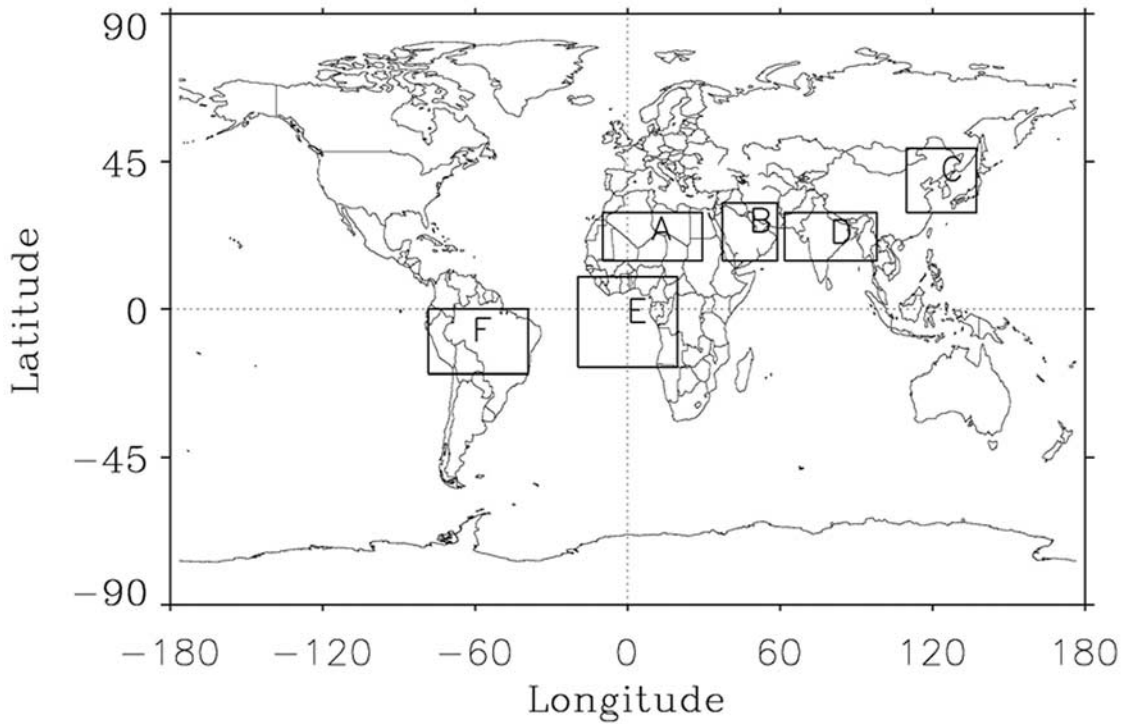


Figure 10. Selected six regions for comparison of AOD for OMI, MODIS, and MISR sensors. The detailed boundaries of each region are described in the text.

from deserts prevail, OMI and MISR show a slightly reduced peak AOD in summer (June and July) compared to that of the Saharan Desert. MODIS shows a peak AOD of 0.6 in July that agrees well with OMI. As in region A OMI tends to overestimate the winter aerosol load relative to MISR and MODIS.

[23] In region C that includes parts of east Asia and the Pacific Ocean, the three instruments show a reasonably good agreement in seasonal cycles within 0.1 AOD. The peak AOD in April is due in part to mineral dust transported from the Taklamakan and Gobi deserts as well as pollution from industrial activities.

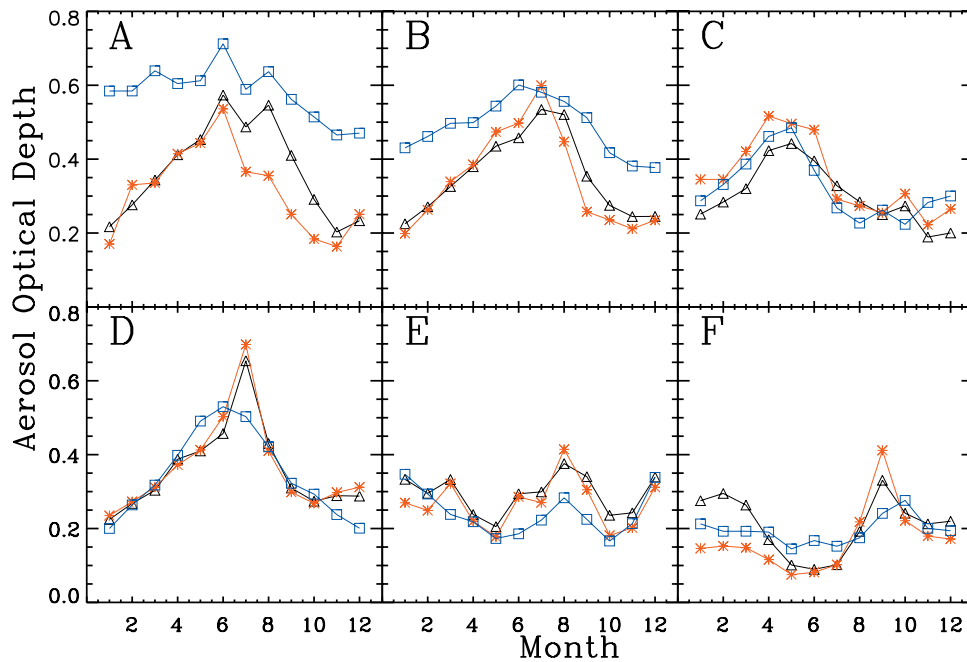


Figure 11. Seasonal variability of monthly AOD in 2006 from Aura/OMI 500 nm (blue squares), Aqua/MODIS 550 nm (red asterisks), and Terra/MISR 558 nm (black triangles) over the selected six regions outlined as A, B, C, D, E, and F in Figure 10.

[24] In region D, over northern India and surrounding areas, the three instruments show a very good agreement except for July, November, and December for which OMI AOD is lower than that of MISR and MODIS.

[25] Region E that includes western equatorial Africa and Atlantic Ocean shows double peaks around summer and winter, which follows a typical semiannual cycle of climate pattern by repeating dry and wet seasons varying with locations of the Intertropical Convergence Zone. Smoke from biomass burning in dry season is washed out during wet season, and shows a strong seasonality in this region. The South American rain forest area (region F) shows the peak in September for both MODIS and MISR, but in October for OMI. These discrepancies of AOD in magnitude and season among three instruments are examined in the following discussion.

[26] Overall monthly AOD means of OMI appear to be higher than those of other two instruments. The systematic high bias is qualitatively consistent with the results of the analysis in section 5. Although several algorithm-related sources of uncertainty can be identified, the most likely reason for most of the observed bias is a calibration offset. Subpixel cloud contamination cannot be discounted as a potentially large source of error in retrieved AOD especially in regions where carbonaceous and pollution aerosols typically coexist with clouds. Over arid and semiarid areas cloud contamination is not expected to be a large source of error. The definition of algorithm flag 0 is empirically determined to minimize subpixel cloud contamination effects so that enough good quality AAOD and AOD data are retained. However, such a simple cloud screening scheme is incomplete to avoid a subpixel cloud contamination issue with varying sizes of footprints as a function of OMI view angles. A restriction of data with flag 0 only in making monthly averages can also result in an overestimate of the monthly means by including in the averages AOD retrievals associated with preferentially large amounts of absorbing aerosols with UVAI above 1.2 than for UVAI below 1.2. Another known source of error in the OMI retrieval is the uncertainty associated with the prescribed aerosol layer height [Torres *et al.*, 1998]. This effect is expected to introduce a random error, and, therefore cannot explain a systematic high bias. With respect to cloud screening techniques, each satellite instrument has its own sampling issues in making monthly averages of AOD [Myhre *et al.*, 2004]. For OMI monthly means, some regions or months show a biased mean estimate due to the paucity of daily samples per month. For example, OMI AOD in November and December over east Asia (region C) tends to be overestimated with respect to MISR and MODIS, because of the average of relatively high AOD from scenes of possibly deficient cloud screening. However, over the Indian subcontinent OMI AOD in July, November, and December is much underestimated compared to other months when good agreement with MISR and MODIS is observed as a result of minimum interference of subpixel cloud contamination. The OMI September underestimation in South America could be explained as the result of a conservative cloud screening (see also AOD map in Figure 8a) that excludes areas of mixtures of broken clouds and aerosols. At their finer spatial resolutions MODIS

and MISR sample the cloud-free spaces to produce AOD retrievals.

8. Summary and Conclusions

[27] New aerosol products (UVAI, AAOD, and AOD) from the EOS Aura/OMI are available for global absorbing aerosol research. These OMI aerosol products are important to provide consistent UVAI and AOD data for the continuity to the TOMS long-term UV observations of absorbing aerosols over both water and land areas. In addition, OMI observations provide a quantitative measure of aerosol absorption not available from any other space-based measurement.

[28] We have compared the OMI retrieved AOD to those of Aqua/MODIS and Terra/MISR sensor by collocation with the OMI footprint. Comparisons were carried out for complete seasonal cycles over regions with typically high-absorbing aerosol loadings in different regions of the world. The three instruments show a fairly reasonable agreement in tracking seasonal annual cycles of aerosol features. These are encouraging results taking into account the large OMI pixel size for which subpixel cloud contamination is unavoidable. Some months and/or regions show sizable differences in magnitude of OMI AOD possibly due to the cloud screening difficulties.

[29] Current large differences between OMI and MODIS, and MISR, especially shown in desert areas such as the Sahara and Arabian deserts where OMI AOD is consistently higher than those of MISR and MODIS, are possibly due to a combination of factors involving cloud contamination, surface albedo effects, radiometric calibrations, and misidentified aerosol type. All of these factors affect the OMI aerosol retrievals with varying degrees of sensitivity under different environmental conditions. Analysis of recently made available recalibrated radiances suggests that a large component of the currently observed biases in the OMI aerosol products can be the result of a calibration offset. Subpixel cloud contamination is the second largest source of error. Other sources of error may contribute to the noise in the retrieval but not necessarily to the systematic bias. Calibration as well as algorithmic issues will be adequately addressed in the next version of the retrieval algorithm and data release. A substantial reduction of the calibration-related errors is expected in Collection 3. As shown in the visual comparisons of UVAI, AAOD, and AOD, three products are complementary to each other for understanding the distribution and magnitude of absorbing aerosols. It is recommended that data users follow the guidelines of algorithm flags presented in this paper. However, the criteria and thresholds can be modified in the next version of reprocessed data sets.

[30] A series of plans are in place to improve the algorithm by reducing the uncertainties in aerosol type selection scheme and vertical distribution of aerosol layer heights through validations with the A-Train data from CALIPSO providing unprecedented information of aerosol layer height distribution, AIRS showing a potential to detect dust type aerosols [DeSouza-Machado *et al.*, 2006], and MODIS providing the Angstrom exponent information that is useful for differentiating sizes of aerosol particles qualitatively [Schuster *et al.*, 2006]. By making use of

collocated A-train observations more accurate information on aerosol layer height and type can be obtained, and a better understanding of the global aerosol distribution and its absorption properties can be achieved.

[31] **Acknowledgments.** We thank the NASA Langley Research Center Atmospheric Science Data Center and Goddard Space Flight Center Level 1 and Atmosphere Archive and Distribution System (LAADS) providing the Terra/MISR and Aqua/MODIS data, respectively. This paper benefited from the invaluable comments of three anonymous reviewers. This work is performed under contract with NASA.

References

- Abdou, W. A., et al. (2005), Comparison of coincident Multiangle Imaging Spectroradiometer and Moderate Resolution Imaging Spectroradiometer aerosol optical depths over land and ocean scenes containing Aerosol Robotic Network sites, *J. Geophys. Res.*, *110*, D10S07, doi:10.1029/2004JD004693.
- Chu, D. A., Y. J. Kaufman, C. Ichoku, L. A. Lemer, D. Tanré, and B. N. Holben (2002), Validation of MODIS aerosol optical depth retrieval over land, *Geophys. Res. Lett.*, *29*(12), 8007, doi:10.1029/2001GL013205.
- DeSouza-Machado, S. G., L. L. Strow, S. E. Hannon, and H. E. Motzler (2006), Infrared dust spectral signatures from AIRS, *Geophys. Res. Lett.*, *33*, L03801, doi:10.1029/2005GL024364.
- Di Girolamo, L., et al. (2004), Analysis of Multi-angle Imaging Spectrometer (MISR) aerosol optical depths over greater India during winter 2001–2004, *Geophys. Res. Lett.*, *31*, L23115, doi:10.1029/2004GL021273.
- Dubovik, O., B. N. Holben, T. F. Eck, A. Smirnov, Y. J. Kaufman, M. D. King, D. Tanre, and I. Slutsker (2002), Variability of absorption and optical properties of key aerosol types observed in worldwide locations, *J. Atmos. Sci.*, *59*, 590–608, doi:10.1175/1520-0469(2002)059<0590:VOAAOP>2.0.CO;2.
- Eck, T. F., et al. (2005), Columnar aerosol optical properties at AERONET sites in central eastern Asia and aerosol transport to the tropical mid-Pacific, *J. Geophys. Res.*, *110*, D06202, doi:10.1029/2004JD005274.
- Herman, J. R., et al. (1997), Global distributions of UV-absorbing aerosols from Nimbus 7/TOMS data, *J. Geophys. Res.*, *102*(D14), 16,911–16,922, doi:10.1029/96JD03680.
- Hsu, N. C., et al. (1999), Comparisons of the TOMS aerosol index and the Sun photometer aerosol optical thickness: Results and applications, *J. Geophys. Res.*, *104*, 6269–6279, doi:10.1029/1998JD200086.
- Hsu, N. C., S.-C. Tsay, M. D. King, and J. R. Herman (2006), Deep blue retrievals of Asian aerosol properties during ACE-Asia, *IEEE Trans. Geosci. Remote Sens.*, *44*, 3180–3195, doi:10.1109/TGRS.2006.879540.
- Kahn, R. A., et al. (2005), Multiangle Imaging Spectroradiometer (MISR) global aerosol optical depth validation based on 2 years of coincident Aerosol Robotic Network (AERONET) observations, *J. Geophys. Res.*, *110*, D10S04, doi:10.1029/2004JD004706.
- Kaufman, Y. J., D. Tanre, L. A. Lemer, E. F. Vermote, A. Chu, and B. N. Holben (1997), Operational remote sensing of tropospheric aerosol over land from EOS moderate resolution imaging spectrometer, *J. Geophys. Res.*, *102*, 17,051–17,067, doi:10.1029/96JD03988.
- King, M. D., Y. J. Kaufman, D. Tanre, and T. Nakajima (1999), Remote sensing of tropospheric aerosols from space: Past, present and future, *Bull. Am. Meteorol. Soc.*, *80*, 2229–2259, doi:10.1175/1520-0477(1999)080<2229:RSOTAF>2.0.CO;2.
- Lau, K. M., and K. M. Kim (2006), Observational relationship between aerosol and Asian monsoon rainfall, and circulation, *Geophys. Res. Lett.*, *33*, L21810, doi:10.1029/2006GL027546.
- Levelt, P. F., E. Hilsenrath, G. W. Leppelmeier, G. H. J. van den Oord, P. K. Bhartia, J. Tamminen, J. F. de Haan, and J. P. Veefkind (2006), Science objectives of the Ozone Monitoring Instrument, *IEEE Trans. Geo. Remote Sens.*, *44*(5), 1093–1101.
- Mahowald, M. N., and J.-L. Dufresne (2004), Sensitivity of TOMS aerosol index to boundary layer height: Implications for detection of mineral aerosol sources, *Geophys. Res. Lett.*, *31*, L03103, doi:10.1029/2003GL018865.
- Myhre, G., et al. (2004), Intercomparison of satellite retrieved aerosol optical depth over ocean during the period September 1997 to December 2000, *Atmos. Chem. Phys. Disc.*, *4*, 8201–8244.
- Schuster, G. L., O. Dubovik, and B. N. Holben (2006), Angstrom exponent and bimodal aerosol size distributions, *J. Geophys. Res.*, *111*, D07207, doi:10.1029/2005JD006328.
- Torres, O., P. K. Bhartia, J. R. Herman, and Z. Ahmad (1998), Derivation of aerosol properties from satellite measurements of backscattered ultraviolet radiation: Theoretical basis, *J. Geophys. Res.*, *103*, 17,099–17,110, doi:10.1029/98JD00900.
- Torres, O., P. K. Bhartia, J. R. Herman, A. Syniuk, P. Ginoux, and B. N. Holben (2002a), A long-term record of aerosol optical depth from TOMS observations and comparison to AERONET measurements, *J. Atmos. Sci.*, *59*, 398–413, doi:10.1175/1520-0469(2002)059<0398:ALTROA>2.0.CO;2.
- Torres, O., R. Decae, J. P. Veefkind, and G. de Leeuw (2002b), OMI aerosol retrieval algorithm, in *Clouds, Aerosols, and Surface UV Irradiance*, vol. 3.2, edited by P. Stammes, *Doc. OMI-ATBD-03*, Goddard Space Flight Cent., Greenbelt, Md. (Available at http://eosps.gsf.nasa.gov/eos_homepage/for_scientists/atbd/docs/OMI/ATBD-OMI-03.pdf)
- Torres, O., A. Tanskanen, B. Veihelman, C. Ahn, R. Braak, P. K. Bhartia, P. Veefkind, and P. Levelt (2007), Aerosols and surface UV products from Ozone Monitoring Instrument observations: An overview, *J. Geophys. Res.*, *112*, D24S47, doi:10.1029/2007JD008809.

C. Ahn, Science Systems and Applications, Inc., 10210 Greenbelt Road, Suite 600, Lanham, MD 20706, USA. (changwoo_ahn@ssaihq.com)

P. K. Bhartia, Goddard Space Flight Center, NASA, 8800 Greenbelt Road, Greenbelt, MD 20771, USA.

O. Torres, Department of Atmospheric and Planetary Sciences, Hampton University, 23 Tyler Street, Hampton, VA 23668, USA.